International Journal of Applied Earth Observation and Geoinformation 130 (2024) 103906

Contents lists available at ScienceDirect

International Journal of Applied Earth Observation and Geoinformation

journal homepage: www.elsevier.com/locate/jag

InSAR and GNSS data fusion for improved urban heat island estimation using local climate zone classification

Melika Tasan [a], Behzad Voosoghi [b], Saeid Haji-Aghajany [c], Mohammad Amin Khalili [d,*], Diego Di Martire [d]

[a] Department of Civil Engineering, Faculty of Environmental Engineering and Geodesy, Wrocław University of Environmental and Life Sciences, 50-363, Wroclaw, Poland
[b] Faculty of Geodesy and Geomatics Engineering, K. N. Toosi University of Technology, Tehran 15433-19967, Iran
[c] Institute of Geodesy and Geoinformatics, Wrocław University of Environmental and Life Sciences, Norwida 25, 50- 375 Wrocław, Poland
[d] Department of Earth, Environmental and Resource Sciences, Monte Sant'Angelo Campus, Federico II University of Naples, 80126 Naples, Italy

ARTICLE INFO

Keywords:
UHI
GNSS
InSAR
LCZ
Temperature

ABSTRACT

The phenomenon of the Urban Heat Island (UHI) is a common feature in city climates, impacting habitat quality and public health. The UHI refers to the temperature difference between metropolitan and countryside areas. This article introduces a new methodology for determining UHI using a high-resolution temperature map created by fusing Interferometric Synthetic Aperture Radar (InSAR) and Global Navigation Satellite Systems (GNSS) measurements. The validity of this method has been assessed by comparing the UHI results with the outputs of the Weather Research and Forecasting (WRF) model. Using the new approach, temperature determination focuses on the moist segment of the tropospheric delay. The wet tropospheric delay is divided into turbulent and non-turbulent components, with the first segment calculated using InSAR and the second using GNSS observations. After generating high-resolution temperature maps to compute the temperature difference between urban and non-urban regions and defining the UHI index, the research area was categorized into various classes based on land cover using the Local Climate Zone Classification (LCZ) approach. Finally, after calculating the UHI in different regions, the results were evaluated against the WRF model outputs. According to the statistical evaluations, the Root Mean Square Error (RMSE) of the UHI index obtained from the novel method and the WRF model outputs ranges from 0.7 to 0.4 Kelvin. The determination coefficient (R^2) also varies from 0.85 to 0.9 in different months. These statistical markers illustrate the significant effectiveness of the suggested technique in computing the UHI phenomenon.

1. Introduction

The UHI phenomenon stems from factors such as sunlight absorption by dark surfaces, air pollution trapping heat, obstructed heat loss by buildings, anthropogenic heat release, increased heat storage in cities, reduced evaporation, and slower heat dispersion due to lower wind speeds (Kleerekoper et al., 2012). While these factors contribute to the surface UHI, it's essential to note that the UHI phenomenon encompasses various types, including atmospheric and canopy UHI, which are not the focus of this paper. In metropolitan zones, it is noticeable that temperatures exceed those in neighboring areas, including rural locales. The UHI phenomenon can affect environmental parameters, including precipitation and the ozone layer (Memon et al., 2009). Research on climate over the past three decades has indicated that extensive urban regions also influence clouds and precipitation (Changnon et al., 1977). As the population grows and cities become more densely built up, the strength of the UHI effect increases (Golden et al., 2007). This leads to higher levels of smog and increased emissions of pollutants from power plants. Additionally, the UHI effect can negatively impact living standards and public health in metropolitan regions. Drawing from prior research, it can be stated that the most important reasons for the UHI phenomenon include the excessive construction of tall buildings, the tremendous heat released by factories and other vehicles that are absorbed by buildings, and population growth in different parts of a city (Liu et al., 2020; Susca & Pomponi, 2020; Kondo et al., 2021). According to this information, measuring and monitoring the UHI is necessary to prevent human life from being affected by this phenomenon.

In modern times, various techniques and instruments, including

* Corresponding author.
E-mail address: mohammadamin.khalili@unina.it (M. Amin Khalili).

https://doi.org/10.1016/j.jag.2024.103906
Received 10 October 2023; Received in revised form 16 April 2024; Accepted 9 May 2024
Available online 19 May 2024

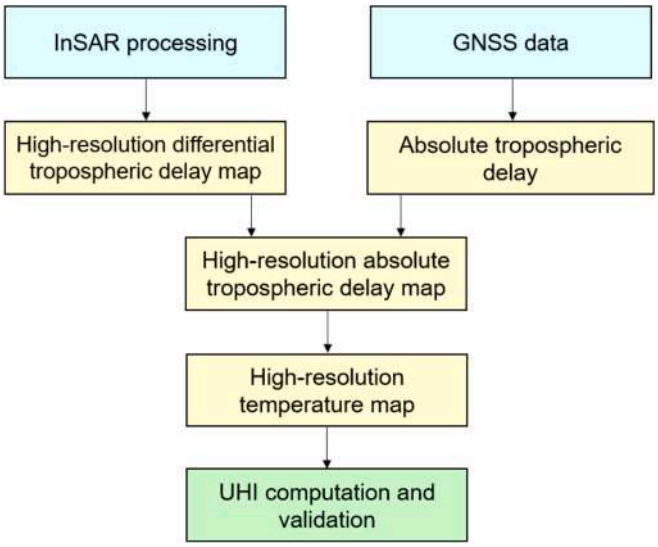

Fig. 1. Flowchart related to the processes of this study.

weather station networks, remote sensing data, numerical weather models, and GNSS data, are employed to measure and monitor UHI (Deilami et al., 2018; Rodríguez et al., 2020; Mendez-Astudillo et al., 2021; Pathak et al., 2021). While weather stations are notably precise instruments for gauging UHI, they are often limited in quantity, resulting in reduced spatial resolution in the final temperature map (Savannah et al., 2011). In contrast, remote sensing satellite data offers high spatial resolution but is sensitive to weather conditions and may not provide accurate data at all times and locations (Mirzaei, 2015). Some researchers have employed a combination of tri-temporal medium-resolution remote sensing imagery, an extended low-resolution surface temperature time series, and high-definition drone imagery to estimate the UHI effect (Cho et al., 2021; Arshad et al., 2022). Airborne instruments have the capability to measure temperature and compute UHI with suitable spatial resolution and high accuracy; however, these instruments are associated with high costs (Sobrino et al., 2012). Numerical weather models offer reasonable accuracy at various spatial resolutions, but they often require significant time for preparation (Giannaros et al., 2013). In previous research, a dynamical downscaling method using a regional climate model was employed to evaluate the UHI effect (Doan et al., 2019). GNSS is another instrument that has gained prominence in recent years for measuring the UHI phenomenon and estimating atmospheric parameters with high temporal resolution and proper accuracy (He et al., 2020; Mendez-Astudillo et al., 2021; Xia et al., 2024). Mendez-Astudillo et al. (2021) introduced a three-step algorithm for monitoring the UHI effect using GNSS data. It addresses the limitations of traditional methods like satellite imagery and airborne sensors. Tested in Los Angeles, the algorithm achieved 1.71 °C accuracy compared to weather station data (Mendez-Astudillo et al., 2021). In the most recent study, researchers proposed an approach by integrating GNSS, space-based GNSS radio occultation, and radiosonde data. The method involves defining grid tops based on historical observations, fitting wet refractivities, estimating temperature and water vapor pressure using GNSS tomography, and evaluating UHI intensity by comparing urban and rural temperatures. Tested in Hong Kong, the approach achieved a 1.2 K accuracy at a 95 % confidence level (Xia et al., 2024). Recent studies show that, due to the limitations of existing instruments and approaches, there is a growing need for a method to prepare temperature maps with both high spatial resolution and accuracy for UHI detection.

In this paper, the authors propose utilizing high spatial resolution radar images and the capabilities of the InSAR technique to measure tropospheric parameters. The proposed approach involves the fusion of InSAR and GNSS data to detect the presence of the UHI phenomenon at a lower cost, independent of weather conditions. The following sections will begin by examining the fundamental principles of the methods employed in this study. Subsequently, the study area and dataset will be introduced. Finally, the subsequent sections will present and evaluate the results.

2. Background and methodology

This section describes the UHI content and formula, the fusion of InSAR and GNSS data to produce a high-resolution temperature map for measuring the UHI, and the validation approaches.

2.1. UHI content

The Urban Heat Island (UHI) is determined by calculating the temperature disparity between rural and urban locations, as defined by Eq.1:

$$UHI = T_{Urban} - T_{Rural} \tag{1}$$

Where, T_{Urban} *and* T_{Rural} represent the urban and rural temperatures, respectively. To compute the UHI using the fusion of InSAR and GNSS data, the following flowchart in Fig. 1 has been used. The flowchart outlines the steps involved in processing and analyzing the data to produce a high-resolution temperature map for measuring UHI.

2.2. InSAR algorithm

InSAR is a well-known and powerful technique across various fields of study, and numerous efforts have been made to utilize and enhance this technique (Miele et al., 2023; Khalili et al., 2023a; Bausilio et al., 2024). The traditional mode of this approach involves analyzing a time series of SAR images obtained from the region to study the changes in deformation over time in each pixel of the satellite image. In the late 1990 s, it was found that some complications displayed constant phase changes over time, leading to the development of the Persistent Scatterer Interferometry (PSI) technique in InSAR processing (Ferretti et al., 2001). This method involves identifying and utilizing Persistent Scatterer (PS) points that exhibit a suitable level of coherency compared to a priori deformation field over time to obtain deformation signals. The process involves using a set of interferograms with multiple SAR images captured over time. The PSI method has been used in many deformation studies and is known for its high accuracy (Ferretti et al., 2001; Hanssen, 2001). Additional details regarding the PSI method are available for those who wish to explore further (Ferretti et al., 2001; Hooper, 2005; Khalili et al., 2023b).

2.3. Extracting absolute turbulent tropospheric wet delay from InSAR

InSAR observations originate from the differential phase between a pair of master and slave images. At each PS point, these observations encompass various phase components, which can be conceptualized as follows (Hanssen, 2001):

$$\Phi^p_{obs} = \Phi^p_{Master} - \Phi^p_{Slave} = \Delta\Phi^p_{def} + \Delta\Phi^p_{top} + \Delta\Phi^p_{atm} + \Delta\Phi^p_{orb} + \Delta\Phi^p_{flat} + \Delta\Phi^p_{noise} \tag{2}$$

Where, p is the PS point number, $\Delta\Phi^p_{def}$ is the phase change related to the ground displacement along the Line Of Sight (LOS) direction, $\Delta\Phi^p_{top}$, $\Delta\Phi^p_{atm}$, $\Delta\Phi^p_{orb}$ and $\Delta\Phi^p_{noise}$ are related to the topographic, atmospheric, orbital, and noise phase, respectively. $\Delta\Phi^p_{flat}$ relates to uncertainties associated with the Earth's ellipsoidal reference surface. After decomposing the atmospheric effect, the relationship can be written as follows:

$$\Phi^p_{obs} = \Delta\Phi^p_{def} + \Delta\Phi^p_{top} + \Delta\Phi^p_{dry} + \Delta\Phi^p_{wet} + \Delta\Phi^p_{ion} + \Delta\Phi^p_{orb} + \Delta\Phi^p_{flat} + \Delta\Phi^p_{noise} \tag{3}$$

Where, $\Delta\Phi^p_{dry}$ and $\Delta\Phi^p_{wet}$ are the hydrostatic and wet parts of the time-related fluctuation of the tropospheric delay elements, respectively. These parameters limit the accuracy of InSAR deformation fields and should be accurately eliminated during different InSAR-based deformation estimation, including earthquakes (Haji-Aghajany et al., 2020) or subsidence (Khalili et al., 2023b). The $\Delta\Phi^p_{ion}$ is the ionospheric phase related to the electron content changes in the ionosphere layer. The deformation phase ($\Delta\Phi^p_{def}$) can be safely disregarded when working with short-temporal baseline interferograms, as long as no significant deformation events transpire during the SAR acquisitions. The topographic phase can be accurately defined by incorporating an external Digital Elevation Model (DEM) into the analysis (Massonnet & Feigl, 1998). Errors in the DEM, ranging from 10 to 20 m, can introduce biases of 0.5 to 1 mm in the final product for C-band. Therefore, the effects of DEM inaccuracies are not significant. The use of Sentinel-1's precision orbit files is employed, providing high-quality satellite trajectory data for the correction of orbital errors.

The ionosphere predominantly exerts its influence on radar signals with long wavelengths, and its impact on the X-band or C-band interferograms remains relatively constrained (Meyer and Nicoll, 2008). Moreover, the ionospheric effect is anticipated to introduce a long-wavelength trend that cannot be distinguished from other phase ramps, and as a result, these effects are typically removed during InSAR processing (Zebker et al., 1997). $\Delta\Phi^p_{dry}$ depends on the time-dependent fluctuation of partial pressure of dry gases and $\Delta\Phi^p_{wet}$ is associated with the time-variant changes in atmospheric water vapor content, which have been the main focus of many of previous studies (Haji-Aghajany & Amerian, 2020a,b; Maddahi et al., 2023). The hydrostatic delay demonstrates minimal temporal shifts due to slight variations in temperature, and the remaining signal, post-interferogram creation, shows linear, long-wavelength spatial fluctuations. As a result, this component is eliminated during the modeling and correction of orbital ramps (Zebker et al., 1997). $\Delta\Phi^p_{noise}$ is the decorrelation noise part that emerges due to the spatio-temporal variability in scattering at a pixel. Decorrelation noise ($\Delta\Phi^p_{noise}$) can be mitigated using spatial filtering methods (Goldstein & Werner, 1998), and its impact on interferograms with short temporal baselines is minimal. Consequently, the component extracted from InSAR interferograms predominantly represents the differential wet delay. To validate InSAR-derived wet delay maps, it is essential to determine which delay components are present in the interferogram and which are not. The wet delay is composed of three parts:

$$Wet\_delay_{Total} = \underbrace{Wet\_delay_{elevation-dependent} + Wet\_delay_{long-wavelength}}_{Non-turbulent\ component} + \underbrace{Wet\_delay_{short-scale}}_{Turbulent\ component} \tag{4}$$

A component dependent on elevation, a long-wavelength element, and a turbulent, short-scale mixed component are involved in InSAR observations. Depending on the surface topography of the study area, the elevation-dependent component may be partially retained or removed in interferograms or during the reduction of the topographic phase (Li et al., 2006; Alshawaf et al., 2014; Haji-Aghajany & Amerian, 2020b). Areas with diverse topography tend to exhibit an elevation-dependent wet delay signal in the interferogram. The long-wavelength component can be challenging to distinguish from orbital ramps, leading to its removal from the interferograms. Conversely, the short-wavelength wet delay component lacks temporal correlation, facilitating its extraction from the interferograms. Consequently, InSAR-derived wet delays encompass short-scale fluctuations, with elevation-dependent and long-wavelength signals excluded. As discussed in the next section, GNSS data will be used to estimate the non-turbulent components. InSAR outcomes represent the difference in wet delays at two distinct times. Therefore, at this stage, estimating the absolute turbulent tropospheric wet delay for each PS point, based on Eq.5, becomes imperative. Eq.1 represents an underdetermined inverse problem, requiring the application of constraints to solve the equation system.

$$\begin{aligned}
\Delta d^1_{1,master} &= d^1_{master} - d^1_1 \\
&\vdots \\
\Delta d^1_{n-1,master} &= d^1_{master} - d^1_{n-1} \\
\Delta d^2_{1,master} &= d^2_{master} - d^2_1 \\
&\vdots \\
\Delta d^2_{n-1,master} &= d^2_{master} - d^2_{n-1} \\
\Delta d^k_{1,master} &= d^k_{master} - d^k_1 \\
&\vdots \\
\Delta d^k_{n-1,master} &= d^k_{master} - d^k_{n-1}
\end{aligned} \tag{5}$$

To confine the inverse problem, it is assumed that the differential delay adheres to a zero-average Gaussian process for each PS point, as depicted in Eq.6 (Alshawaf, 2013). After adding these constraints to the equation, a well-defined inverse problem can be constructed, as detailed in Eq.7 and Eq.8.

$$\begin{aligned}
&\sum_{i=1}^{n} \frac{1}{n} d^1_i = 0 \\
&\vdots \\
&\sum_{i=1}^{n} \frac{1}{n} d^k_i = 0
\end{aligned} \tag{6}$$

$$\overbrace{\begin{bmatrix} -1 & 0 & \dots & +1 & 0 & \dots & 0 \\ 0 & -1 & \cdots & +1 & 0 & \dots & 0 \\ \vdots & \vdots & \cdots & \vdots & \vdots & \dots & \vdots \\ 0 & 0 & \cdots & +1 & 0 & \dots & -1 \\ \frac{1}{n} & \dots & \dots & \frac{1}{n} & \dots & \dots & \frac{1}{n} \end{bmatrix}}^{A} \overbrace{\begin{bmatrix} d^k_1 \\ \vdots \\ d^k_{master} \\ \vdots \\ d^k_n \end{bmatrix}}^{X} = \overbrace{\begin{bmatrix} \Delta d^k_{1,master} \\ \vdots \\ \vdots \\ \Delta d^1_{n-1,master} \\ 0 \end{bmatrix}}^{L} \tag{7}$$

$$\boldsymbol{X}_{n\times k} = \left(\boldsymbol{A}^T_{n\times n}\boldsymbol{A}_{n\times n}\right)^{-1}\boldsymbol{A}^T_{n\times n}\boldsymbol{L}_{n\times k} \tag{8}$$

Where k, n, and d^k_{n-1} are the number of PS points, the number of radar images and the partial wet delay at the location of kth PS in the n-1th image, respectively. A represents the design matrix, L is the matrix comprising turbulent differential tropospheric wet delay, and X embodies the matrix of turbulent absolute tropospheric wet delay for each PS in every image. The resolution for Eq.7 is derived by utilizing the Least Squares (LSQ) inversion principle, based on Eq.8. It's pertinent to mention that the InSAR wet delays are oriented along the LOS direction of the radar satellite, which deviates from the GNSS satellites' direction. Consequently, it is imperative to project the InSAR outcome into the zenith direction. Past studies have validated that utilizing an incidence angle for each PS point is adequate (Alshawaf et al., 2014).

2.4. Extracting absolute non-turbulent tropospheric wet delay from GNSS

The tropospheric delay is generally known as an intruder effect on GNSS positioning, and a lot of effort has been made to reduce this impact using different methods like ray-tracing techniques (Haji-Aghajany & Amerian, 2018) and troposphere tomography (Haji-Aghajany, 2021; Haji-Aghajany et al., 2021). From a different perspective, this intruder effect in positioning proves valuable in some other fields. GNSS

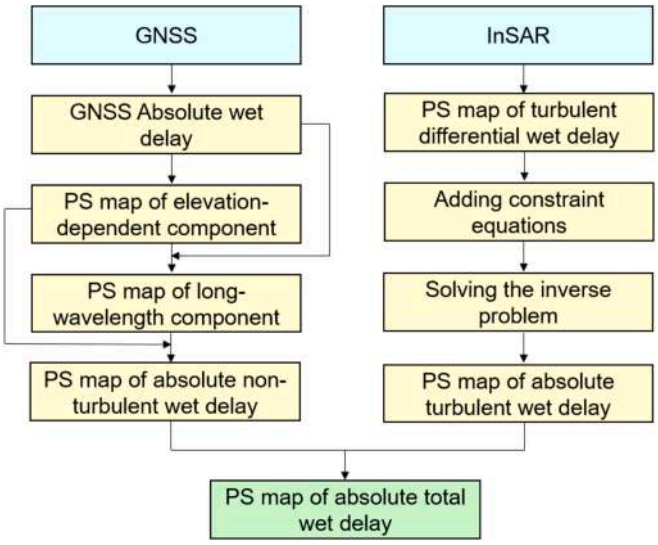

Fig. 2. Flowchart to compute wet delay using the fusion of InSAR and GNSS data.

tropospheric products are widely used in various fields of study, including troposphere tomography (Haji-Aghajany, 2021; Izanlou et al., 2024), machine learning-based land subsidence prediction (Tasan et al., 2023), and machine learning-based groundwater level prediction (Haji-Aghajany et al., 2023). As previously noted, in this paper, GNSS data is utilized to calculate the non-turbulent segments of the tropospheric wet delay. Fig. 2 shows the procedure of estimating absolute wet delay using fusion of InSAR and GNSS measurements. The overall tropospheric delay along the zenith direction is initially derived from GNSS processing to calculate the absolute wet delay from GNSS data (Haji-Aghajany et al., 2021, 2022). Then, the dry part is subtracted from the total delay using a precise empirical model called the Saastamoinen model (Saastamoinen, 1973). In order to model the elevation-dependent component an exponential function is used (Onn & Zebker, 2006):

$$delay_{elevation-dependent} = ae^{(-bH)} + abHe^{(-bH)} + c \tag{9}$$

Where H refers to the altitude and a, b, and c are the model parameters that will be calculated utilizing GNSS station measurements. To measure the goodness of fitting, the reduced chi-squared statistic is used (Onn & Zebker, 2006). After fitting the model and computing the final residual, the other non-turbulent component of wet delay related to the long-wavelength effect can be estimated. For this purpose, the elevation-dependent component will be deducted from the total wet delay estimated from GNSS measurements. Then, a linear model will be fitted to the residual to estimate the long-wavelength component:

$$delay_{long-wavelength} = p\varphi + q\lambda + r \tag{10}$$

Where φ and λ are referring to the geographical coordinates of the GNSS station (latitude and longitude), and p, q, and r are the model components. The non-turbulent element of the wet delay can be determined by adding the long-wavelength and elevation-dependent components. As illustrated in Fig. 2, the comprehensive tropospheric wet delay can be calculated by combining the InSAR turbulent component from InSAR with the non-turbulent component derived from GNSS measurements. It should be mentioned that the Kriging interpolation technique is used to interpolate GNSS outputs on PS coordinates.

2.5. High-resolution temperature map

Based on previous studies and the physical aspects of signal transmission through the troposphere, the Zenith Tropospheric Delay (ZTD) and its two components, Zenith Hydrostatic Delay (ZHD) and Zenith Wet Delay (ZWD), can be expressed as follows (Nilsson et al., 2013):

$$ZTD = ZHD + ZWD = 10^{-6}\int_{h_{Station}}^{h_{Troposphere}} N\,ds = 10^{-6}\int_{h_{Station}}^{h_{Troposphere}} (N_{hyd} + N_{wet})ds \tag{11}$$

$$N = \underbrace{k_1\frac{R}{M_d}\rho}_{N_{hyd}} + \underbrace{k_2'\frac{e}{T}Z_w^{-1} + k_3\frac{e}{T^2}Z_w^{-1}}_{N_{wet}} \tag{12}$$

$$ZWD = 10^{-6}\int_{h_{Station}}^{h_{Troposphere}} (k_2'\frac{e}{T}Z_w^{-1} + k_3\frac{e}{T^2}Z_w^{-1})\,ds \tag{13}$$

Where N, N_h and N_w are total hydrostatic and wet refractivity, respectively. The ds is the distance between the receiver and the top of the troposphere,k_1, k_2' and k_3 are the frequency-dependent empirical coefficients, ρ is the density of dry air, M_d is the molar mass for dry air, R is the universal gas constant, Z_w is the compressibility factors for water vapor, e is the water vapor pressure and T is temperature. Due to the fact that the meteorological data is distributed at different and discrete pressure levels, in operational mode, the integral is discretized as follows:

$$ZWD = 10^{-6}\sum_{i=1}^{Np-1}(k_2'\frac{e_m^i}{T_m^i}Z_w^{-1} + k_3\frac{e_m^i}{(T_m^i)^2}Z_w^{-1})(h_{i+1} - h_i) \tag{14}$$

$$e_m^i = \frac{e_i + e_{i+1}}{2}\ ,\ T_m^i = \frac{T_i + T_{i+1}}{2} \tag{15}$$

Where N_p is the number of pressure levels regarding the numerical weather models and e_m^i and T_m^i are water vapor and temperature between two consecutive pressure levels. It is notable that e^1 and T^1 represent the water vapor pressure and temperature near the surface, respectively. The water vapor pressure at various heights can be calculated utilizing Antoine's model, which is grounded in the Clausius-Clapeyron relation for gases (Tolman, 2008):

$$e^i = \frac{10^{A-\frac{B}{C+T^i}}}{0.75} \tag{16}$$

Where A, B and C are Antoine's constants (A = 8.071, B = 1730.63 and C = 233.43). This model is valid for temperatures between 0 °C and 100 °C. It is assumed that temperatures in the big city are in this range. When temperatures fall below 0 °C, water vapor pressure drops to zero because water molecules freeze and do not evaporate. On the other hand, the temperature in different vertical layers can be estimated using an empirical formula (Mendes and Langley, 1998):

$$T^{i+1} = T^i - \beta(h^{i+1} - h^i) \tag{17}$$

Where β is a coefficient that is computed using radiosonde measurements in the study area. Upon implementing Eq.15, Eq.16, and Eq.17 into Eq.14, the sole unidentified parameter becomes the surface temperature. Consequently, a high-resolution temperature map will be redeveloped.

2.6. Classification of the study area

As discussed in the preceding section, the UHI represents the temperature disparity between rural and urban regions. Therefore, one of the crucial steps in estimating UHI is differentiating between various segments of the study area. The use of the LCZ classification becomes essential for segregating urban and rural zones based on their adjacent land cover (Stewart & Oke, 2012; Stewart et al., 2014). While the traditional LCZ classification method relies on ground-based

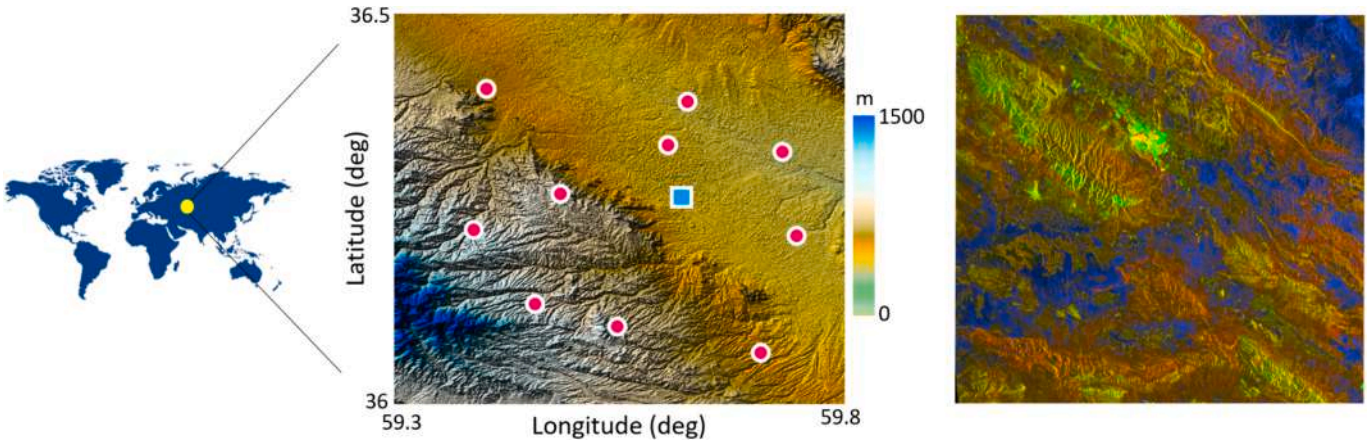

Fig. 3. The geographic location and a sample of the radar scene of the study area.

Table 1
Specifications of Sentinel-1A radar acquisitions.

Mission	Product	Track	Flight Direction	Beam Mode	Time period
Sentinel-1A	S1A-IW-SLC	93	DESCENDING	IW	Jan 2022 to Dec 2022

observations, satellite imagery can also be employed to categorize LCZ types across extensive areas. This approach offers a cost-effective means to analyze the spatial distribution of urbanization and its impact on the local climate. Satellite images provide high-resolution spatial data on the land cover surrounding a region of interest, such as a city or a larger area. This information can be used to classify the area into different LCZ categories, which describe the physical properties of the land cover and their influence on the local climate (Demuzere et al., 2021; Demuzere et al., 2022). Satellite-based LCZ classification is particularly useful for monitoring urbanization trends and their environmental effects over time. One advantage of this approach is its ability to classify areas that are difficult or impossible to access on the ground, such as remote regions or areas with restricted access.

2.7. Validation methods

Generally, statistical parameters, including the RMSE, Nash-Sutcliffe Efficiency (NSE), R^2, and Mean Absolute Error (MAE), are utilized to assess the acquired UHI. These parameters are calculated as follows (Moriasi et al., 2007):

$$RMSE = [\frac{1}{n}\sum_{i=1}^{n}(S_i - O_i)^2]^{\frac{1}{2}} \tag{18}$$

$$NSE = 1 - \frac{\sum_{i=1}^{n}(O_i - S_i)^2}{\sum_{i=1}^{n}(O_i - \overline{O})^2} \tag{19}$$

$$R^2 = \left[\frac{\frac{1}{n}\sum_{i=1}^{n}(S_i - \overline{S})(O_i - \overline{O})}{\sigma_s \times \sigma_o}\right]^2 \tag{20}$$

$$MAE = \frac{\sum_{i=1}^{n}|S_i - O_i|}{n} \tag{21}$$

where S_i and O_i are the modeled and observed data, $\overline{S}$ and $\overline{O}$ are the average of the modeled and observed data, and σ_S and σ_O are the standard deviation of the modeled and observed data, respectively. RMSE is a measure of the difference between modeled and observed values. NSE quantifies the model's proficiency in mirroring the observed data. It's calculated by squaring the deviation between the modeled and observed values, then dividing by the square of the variance between the observed and mean values. NSE spans a range from negative infinity to 1, with a score of 1 denoting a perfect match between modeled and observed values. R^2 signifies the percentage of variance in the observed data that is accounted for by the model, ranging from 0 to 1, where 1 implies the model comprehensively explains the data's variability. Meanwhile, MAE provides a measure of the average absolute divergence between the modeled and observed values.

3. Study area and data sets

Mashhad, Iran's second-largest city, is situated in the country's northeastern region. As of the most recent 2021 data, its population is approximately 3.5 million. Climate-wise, Mashhad endures a semi-arid environment with hot summers and chill winters. There is a noteworthy diurnal temperature variation, with winter temperatures (December through February) often plummeting below freezing and averaging between 0 °C and 15 °C. The summer, spanning June to August, brings hot, dry conditions, with mean temperatures oscillating between 20 °C and 35 °C. Positioned 985 m above sea level, Mashhad spans 431 square kilometers. In 2019, the city welcomed about 2.5 million international tourists, according to the Statistical Center of Iran (2018). A 2021 report from Iran's Environmental Protection Agency indicated that Mashhad's air pollution, notably for fine particles and sulfur dioxide, surpassed national benchmarks (Tehran Times, 2023). Fig. 3 illustrates the geographic locale of the study area. It's vital to note that the region has not recorded any tectonic activity during the investigative period.

For the research, several Sentinel-1A radar captures from the study area were utilized to apply the InSAR technique. Radar acquisition specifications are detailed in Table 1. To estimate the non-turbulent component of the tropospheric wet delay, ten GNSS stations were employed. Additionally, readings from a radiosonde station in the study zone were used to determine the coefficient of Eq.16. The layout of GNSS stations and the radiosonde station's location are visualized in Fig. 3.

In this study, the outcomes are validated using the WRF model, a numerical weather prediction system known for its ability to simulate surface temperatures with high spatial and temporal precision. It can generate hourly surface temperature outputs at kilometer-scale spatial resolution (Michalakes et al., 2004). Meteorological forecasts required for running the WRF model are obtained from Global Forecast System analysis (GFS) data.

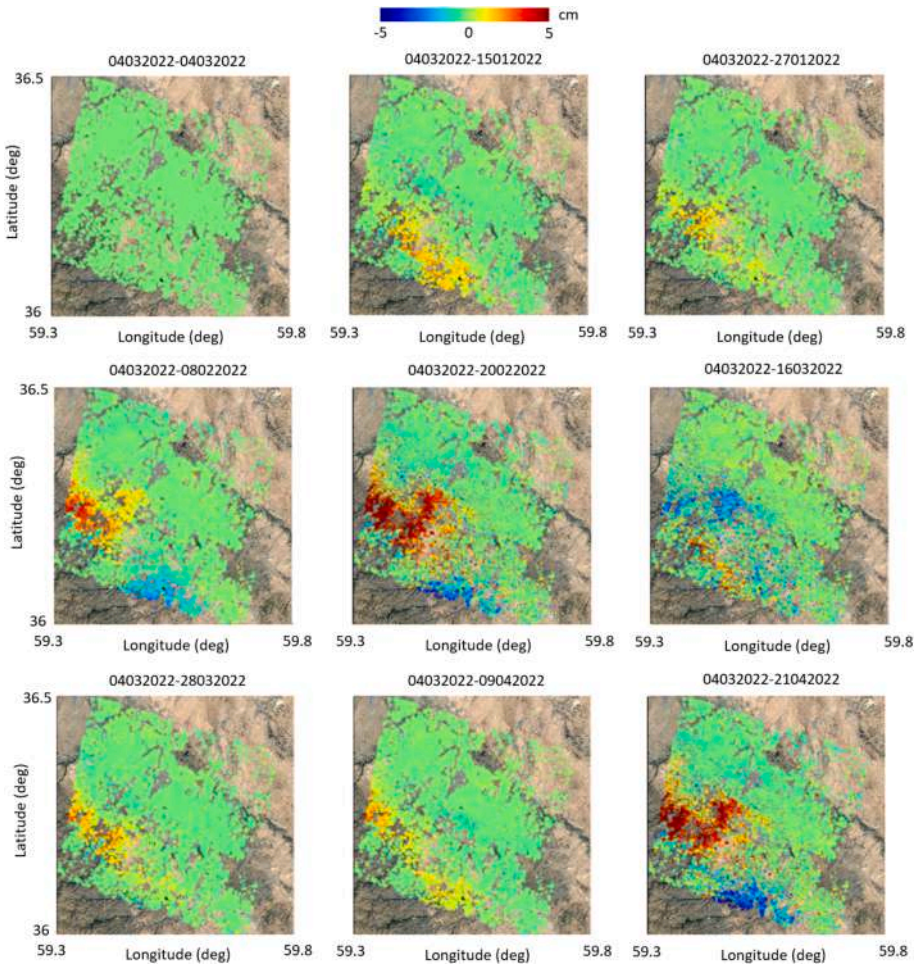

Fig. 4. Sample of obtained turbulent differential wet delay maps from InSAR. The date 04,032,022 has been considered as the master date.

4. Processing results and analysis

This section will describe the processes used in the study and present the obtained results, which will be evaluated accordingly. Firstly, the results of the area classification will be presented, followed by the results related to temperature maps. Finally, the heat island phenomenon will be evaluated and discussed.

4.1. Temperature map

As mentioned in the theoretical part of the paper, the first step is to extract the turbulent part of the tropospheric delay using InSAR observations. Interferograms with spatial baselines of up to fifty days were obtained to achieve this aim. The selection of the master acquisition was based on having the minimum level of incoherence, meaning that the chosen image should exhibit the least amount of vertical, temporal, and Doppler baseline differences compared to the others (Hooper, 2005). Due to the absence of deformation in the area and correction of other effects in the interferograms as described in previous sections, the obtained interferograms only contain the turbulent differential tropospheric delays. A sample of the findings is visible in Fig. 4. The southern regions of the area exhibit a more pronounced discrepancy in the turbulent portion, escalating up to 5 cm, while the disparity in the northern parts is comparatively subdued.

The equations of the obtained observations were solved based on added constraints to obtain the turbulent absolute tropospheric delays for each acquisition time. The obtained results have been projected in the zenith direction to combine them with GNSS measurements. Once all the necessary outputs from InSAR were obtained, the missing parts of the tropospheric wet delay were calculated using GNSS observations and added to the previous values. The Bernese 5.2 software was utilized for GNSS data processing, employing the Precise Point Positioning (PPP) method to derive the zenith direction tropospheric delay. This was achieved with a temporal resolution of one hour for each day radar data was acquired (Dach et al., 2015).

Upon calculating the total tropospheric delay, the wet delay was determined by employing the Saastamoinen model to exclude the dry component. The delay values were then interpolated on the PS points using the Kriging method. Leveraging the aforementioned relations, the elevation-dependent and long-wavelength segments of the wet delay were evaluated, resulting in the reconstruction of high-resolution absolute tropospheric wet delay maps. Once the tropospheric wet delay was calculated at the PS points, the surface temperature was determined using the method described in Section 2.5. The temperature variable was calculated by converting Eq.14 into a single-variable equation. Fig. 5 shows examples of temperature maps calculated using InSAR data and GNSS observations, displaying the calculated temperature for one day of each month in 2022. The maps indicate that the temperature initially increased and then decreased towards the end of the year. It should be noted that in Fig. 5, colorbars with different ranges have been used because the temperature range varies at different dates. If the same colorbar were used for all subfigures, the temperature difference in different parts of the area would not be visible on some dates.

The highest temperature in the area was observed in June, reaching 320 degrees Kelvin, and in July, the southeast of the study area also showed high temperatures. The months of November and December

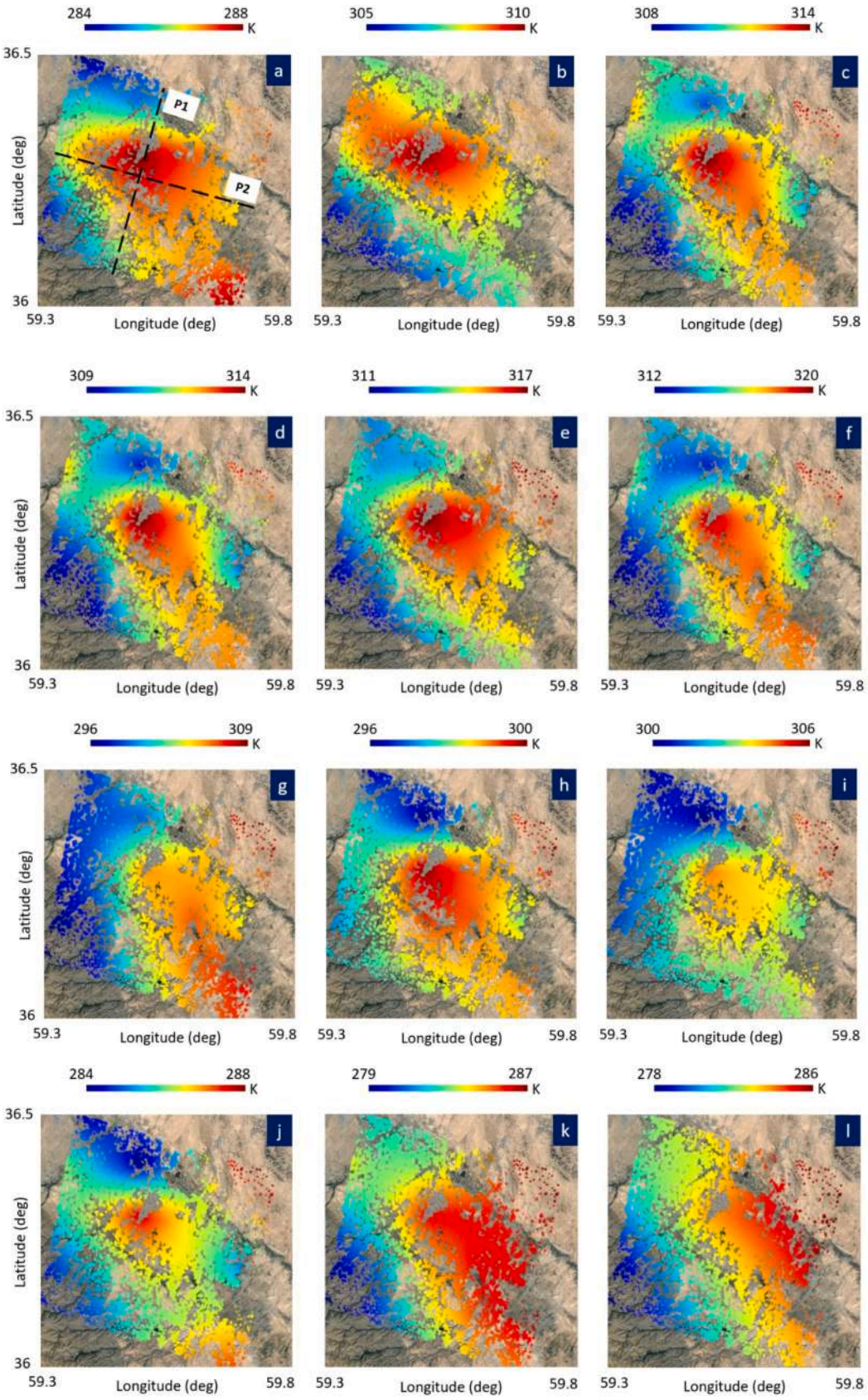

Fig. 5. Sample of obtained temperature map from the fusion of InSAR and GNSS data. The dashed lines show the considered profiles to better express the temperature difference. The labels "a" to "l" correspond to the different months from January to December in the year 2022.

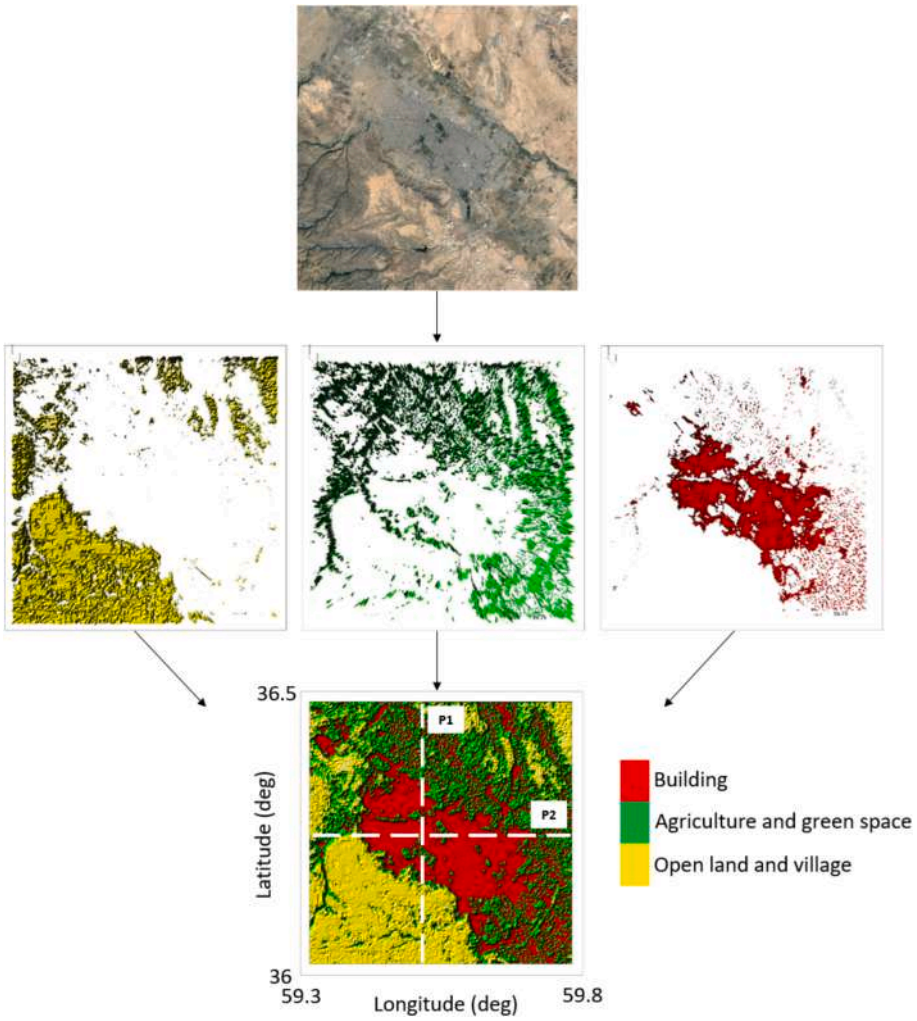

Fig. 6. Classification of the study area and considered profiles.

exhibited the lowest average temperatures. The maps further reveal that the central region, an urban zone, consistently exhibited higher temperatures than its surroundings across all months. In both October and August, the temperature disparity among different portions of the region was less pronounced compared to other months, with the peak temperature variance approximating 4 degrees Kelvin. The highest temperature differences in various PS points in the study area occurred in June, July, November, and December, with differences reaching up to 13 degrees Kelvin. Two profiles on the maps were considered to assess spatial temperature variations, which will be analyzed in the following sections. The integration of InSAR and GNSS data resulted in high-resolution temperature maps. However, the obtained results require validation using credible external data.

4.2. Classification of the area

The LCZ Generator, devised by Demuzere et al. (2021), was utilized to classify LCZs, adhering to the standard procedure of the World Urban Database and Access Portal Tools. This was executed by utilizing Landsat data and amalgamating Sentinel-1, Sentinel-2, DEM, global forest canopy height, and additional earth observation data via the random forest algorithm. The LCZ Generator facilitates easy quality control by enabling the user to generate classification results (Demuzere et al., 2021; Demuzere et al., 2022). Utilizing this instrument, the study area can be categorized into 17 distinct classes, anchored in vegetation types and building coverage. The objective of this research is to calculate the temperature discrepancy between urban and rural segments. Therefore, in this study, the area has been classified into three different classes: buildings, comprising various densities and heights; agriculture and green space, encompassing different types of vegetation cover such as forests, parks, and agricultural fields; and open land and village areas, including sparsely built areas, bare rock or paved surfaces, bare soil or sand, and water bodies. The classified area derived from the information in 2022 is visible in Fig. 6, where the urban zone is situated at the center of the map. The agricultural area, together with green space, is situated around the city, while the open land and village class can be seen around the edges of the map. By using this classification method, it is possible to separate the PS points into different classes and measure the UHI phenomenon.

4.3. UHI results and discussion

After reconstructing the high-resolution temperature map and classifying the study area, it is now essential to explore and assess the UHI effect within the research area. To achieve this, two profiles, as seen in Fig. 5 and Fig. 6, have been selected on the obtained maps. Along these profiles, all three types of land cover, including building, agriculture and green space, and open land and village, have been considered. Therefore, the UHI can be studied based on the temperature changes along these profiles. The temperature variations are visible in Fig. 7. It is worth noting that these graphs have been drawn based on the obtained temperature maps shown in Fig. 5. In every chart, the UHI effect is evident

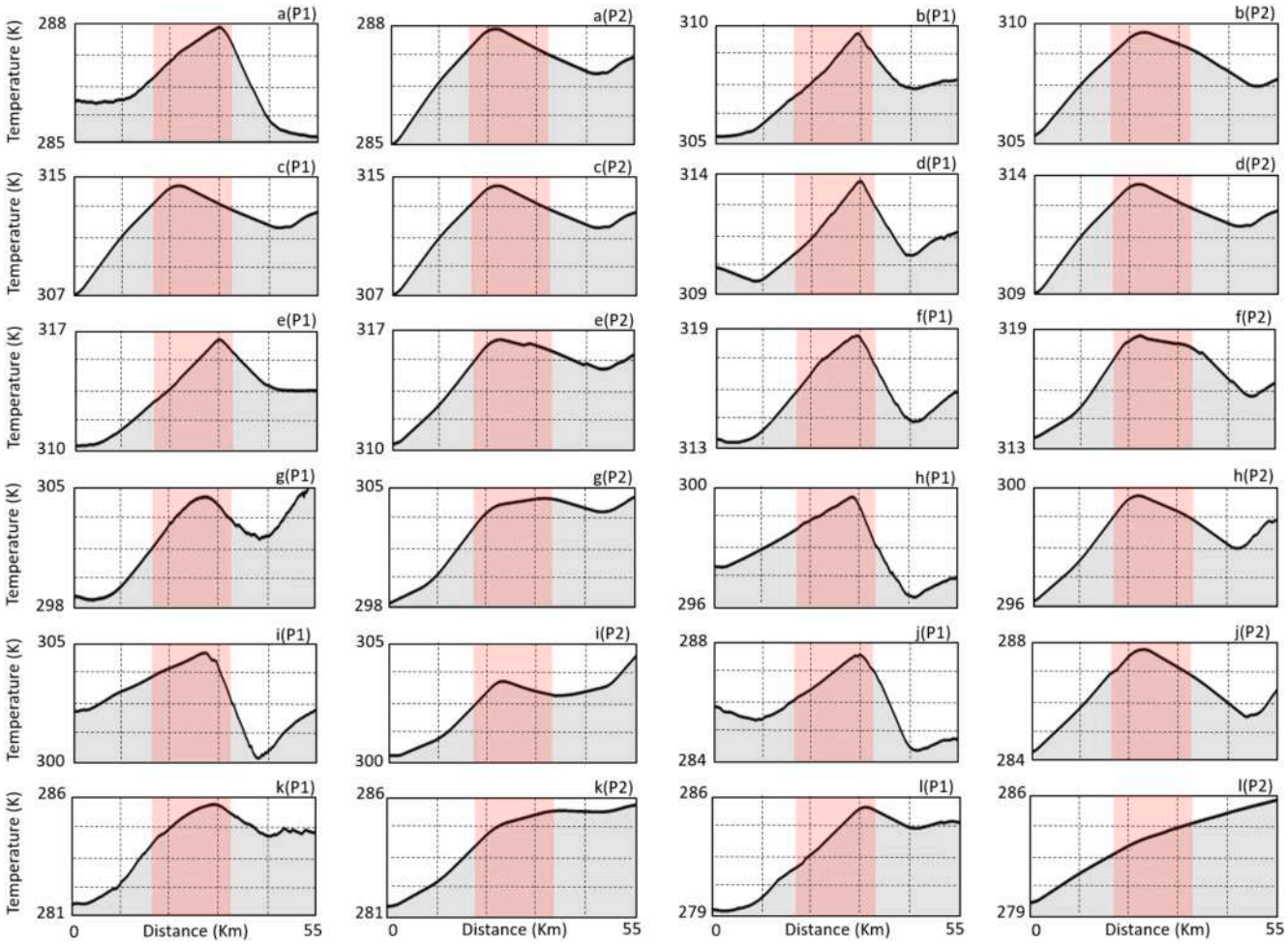

Fig. 7. Temperature variations were analyzed along two selected profiles on different dates, as shown in Fig. 6. The red rectangle indicates the urban area, while labels "a" to "l" correspond to the different months from January to December in the year 2022. Additionally, labels "P1″ and "P2″ denote profile 1 and profile 2, respectively. (For interpretation of the references to colour in this figure legend, the reader is referred to the web version of this article.)

Table 2
The physics schemes used in the WRF configuration.

Category	Scheme	Reference
Shortwave radiation	Rapid Radiative Transfer Model forGlobal climate models (RTMG)	(Iacono et al., 2008)
Longwave radiation	RTMG	(Iacono et al., 2008)
Planetary boundary layer	Mellor-Yamada and Nakanishi-Niino	Nakanishi and Niino (2006)
Land surface	Noah-MP (multi-physics)	(Niu et al., 2011)
microphysics	Thompson	Thompson et al. (2008)

owing to the significant temperature discrepancy between the urban zones and other regions. In other words, the peak point of the graphs is seen in the urban area, and before and after that, the graph shows a descending trend. In the graphs related to January, which are shown with label a, the urban heat island phenomenon is more apparent along profile P1 than P2. This value reaches about 3 degrees Kelvin. In the February graphs, denoted with label b, temperature variations maintain consistency across both profiles, with the temperature differential between urban and non-urban zones reaching up to 5 degrees Kelvin.

Based on the available graphs, the existence of the UHI phenomenon in the area is apparent. In March (c), similar changes in both profiles are visible, and the UHI has had a significant increase compared to the

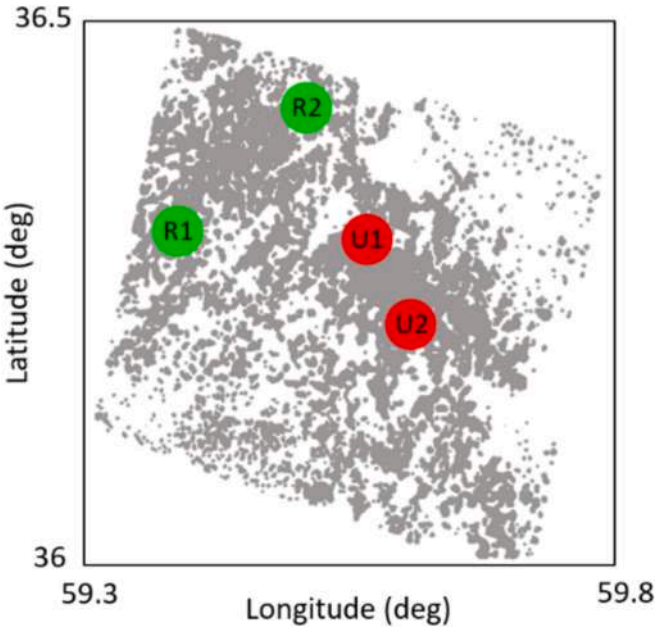

Fig. 8. Considered parts for statistical comparison. "U" and "R" refer to urban and rural areas, respectively.

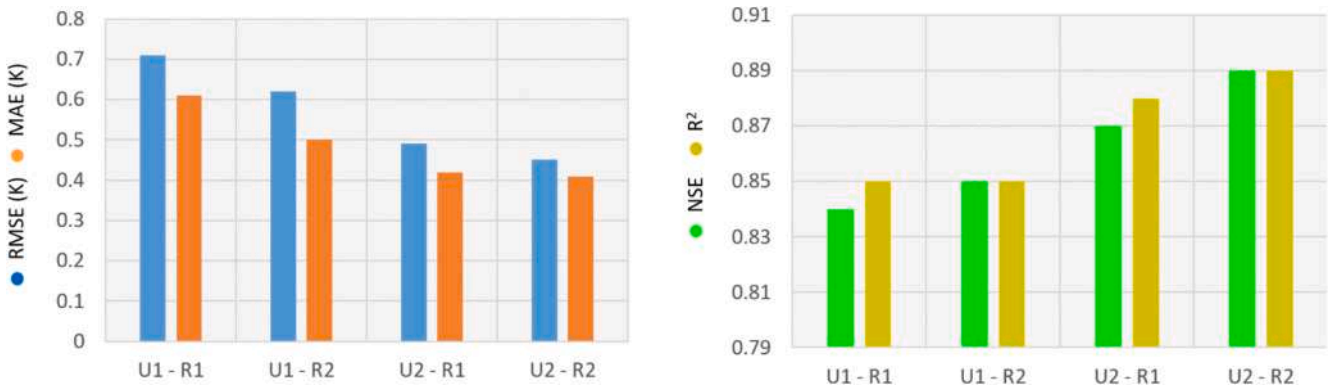

Fig. 9. Statistical comparison of the results.

Table 3
Comparing obtained UHI with WRF model output.

UHI	RMSE (K)	MAE (K)	NSE	R^2
U1 – R1	0.71	0.61	0.84	0.85
U1 – R2	0.62	0.50	0.85	0.85
U2 – R1	0.49	0.42	0.87	0.88
U2 – R2	0.45	0.41	0.89	0.89

previous two months, reaching 8 degrees Kelvin. Also, in April (d), May (e), June (f), and July (g), the value of this phenomenon is variable between 5 and 7 degrees Kelvin. It is worth mentioning that in graph g, following the traverse through the urban area, the decline in temperature is less pronounced compared to other instances. Generally, it can be said that the behavior of the profiles after passing through the urban area is different from their behavior before reaching this area. The phenomenon also decreases as the winter season approaches and the average temperature decreases in the area.

In summary, the minimal intensity of the UHI is discernible during the colder months. To validate the accuracy of the outcomes derived from merging InSAR and GNSS data—utilizing a novel methodology for acquiring high-resolution temperature maps—it is imperative to assess the results against trustworthy output data.

The surface temperature derived from the WRF model was employed to validate the results. However, it should be noted that the radiosonde measurements were not utilized for the evaluation of the obtained temperature as they were only applied to determine a coefficient in Eq.17. The WRF model was executed with two nested domains situated within a primary domain, and Table 2 showcases the array of physics schemes employed in the model. To compare the results with the WRF outputs, four different areas, including urban and rural regions, were considered. As shown in Fig. 8, these parts are represented as circles with a radius of 10 km. The WRF outputs were estimated at a spatial resolution of 1 km. The temperature values used in the comparison were obtained from the temperature average within each circle. Fig. 9 and Table 3 indicate the statistical analysis of obtained temperature. It is evident that the UHI values garnered from the innovative method have been compared with the outputs derived from the WRF model across diverse segments of the area. The maximum RMSE value is 0.7 Kelvin, while the minimum value is around 0.4 Kelvin.

Additionally, the maximum value of MAE is 0.6 Kelvin, indicating a high consistency between the obtained results and the outputs of the WRF model. The peak value for the NSE coefficient is approximately 0.89, while the lowest figure hovers around 0.85. The R^2 also shows values between 0.85 and 0.89. The proximity of these values to 1 indicates the consistency of the results with the WRF model outputs.

5. Conclusions

This paper proposed a novel approach for calculating the UHI effect by utilizing a high-resolution temperature map generated by integrating InSAR data with GNSS measurements, which is independent of weather conditions. The temperature of the region was deduced by considering the wet part of the tropospheric delay, which is segmented into turbulent and non-turbulent portions. The turbulent part was calculated using InSAR, while the non-turbulent part was calculated using GNSS observations. The proposed method provides a suitable approach to reconstructing high-resolution temperature maps and calculating the UHI phenomena. After generating high-resolution temperature maps, The UHI index was ascertained by computing the temperature discrepancy between urban and non-urban zones. The study area was then classified into different land coverage classes using the LCZ method, which enables an understanding of the spatial distribution of the UHI. The obtained UHI results were evaluated by comparing them with the outputs of the WRF model, and statistical assessments revealed that the suggested technique exhibits commendable efficacy. The RMSE of the UHI index obtained from the novel method and WRF model was between 0.7- and 0.4-degrees Kelvin, while the MAE parameter was between 0.41 and 0.61. Furthermore, the NSE varied from 0.85 to 0.9 in different months of the year, with the R^2 index ranging from 0.85 to 0.89. Utilizing InSAR and GNSS measurements allows a more accurate assessment of the UHI effect in urban areas. Furthermore, utilizing the LCZ method to categorize the research area into varied land cover classes also yields significant insight into the UHI's spatial distribution.

CRediT authorship contribution statement

Melika Tasan: Conceptualization, Formal analysis, Methodology, Writing – original draft. **Behzad Voosoghi:** Supervision. **Saeid Haji-Aghajany:** Conceptualization, Software, Writing – original draft, Writing – review & editing. **Mohammad Amin Khalili:** Formal analysis, Software. **Diego Di Martire:** Supervision.

Declaration of competing interest

The authors declare that they have no known competing financial interests or personal relationships that could have appeared to influence the work reported in this paper.

Data availability

The authors do not have permission to share data.

Acknowledgments

This study was carried out within the RETURN Extended Partnership

and received funding from the European Union Next-GenerationEU (National Recovery and Resilience Plan – NRRP, Mission 4, Component 2, Investment 1.3 – D.D. 1243 2/8/2022, PE0000005). The authors would like to appreciate the European Space Agency (ESA) for providing the radar acquisitions. Detailed and constructive reviews and editorial remarks are greatly appreciated.

References

Alshawaf, F., 2013. Constructing water vapor maps by fusing InSAR, GNSS, and WRF data. Karlsruhe Institute of Technology, Karlsruhe, Germany. PhD thesis.

Alshawaf, F., Hinz, S., Mayer, M., Meyer, F.J., 2014. Constructing accurate maps of atmospheric water vapor by combining interferometric synthetic aperture radar and GNSS observations. J. Geophys. Res. Atmos. 120, 1391–1403. https://doi.org/10.1002/2014JD022419.

Arshad, S., Ahmad, S.R., Abbas, S., Asharf, A., Siddiqui, N.A., Islam, Z.U., 2022. Quantifying the Contribution of Diminishing Green Spaces and Urban Sprawl to Urban Heat Island Effect in a Rapidly Urbanizing Metropolitan City of Pakistan[j]. Land Use Policy 113, 105874. https://doi.org/10.1016/j.landusepol.2021.105874.

Bausilio, G., Khalili, M.A., Virelli, M., Di Martire, D., 2024. Italian COSMO-SkyMed atlas: R-Index and the percentage of measurability of movement. Giscience & Remote Sensing 61 (1). https://doi.org/10.1080/15481603.2024.2312705.

Changnon Jr., S.A., Huff, F.A., Schickendanz, P.T., Vogel, J.L., 1977. Summary of METROMEX, Vol. Weather anomalies and impacts. Illinois State Water Survey Bull. 62, 260 pp.

Cho, Y.I., Yoon, D., Shin, J., Lee, M.-J., 2021. Comparative Analysis of the Effects of Heat Island Reduction Techniques in Urban Heatwave Areas Using Drones[j]. Korean J. Remote Sens 37 (6_3), 1985–1999.

Dach R, S Lutz, P Walser, P. Fridez. (2015), Bernese GNSS Software Version 5.2. User manual, Astronomical Institute, University of Bern, Bern Open Publishing. DOI: https:// doi. org/ 10. 7892/ boris. 72297; ISBN: 978–3–906813–05–9.

Deilami, K., Kamruzzaman, M., Liu, Y., 2018. Urban heat island effect: A systematic review of spatio-temporal factors, data, methods, and mitigation measures. Int J Appl Earth Obs Geoinf 67, 30–42. https://doi.org/10.1016/j.jag.2017.12.009.

Demuzere, M., Kittner, J., Bechtel, B., 2021. LCZ Generator: A Web Application to Create Local Climate Zone Maps. Front. Environ. Sci. 9, 637455.

Demuzere, M., Kittner, J., Martilli, A., Mills, G., Moede, C., Stewart, I.D., van Vliet, J., Bechtel, B., 2022. A global map of local climate zones to support earth system modelling and urban-scale environmental science. Earth Syst. Sci. Data 14, 3835–3873. https://doi.org/10.5194/essd-14-3835-2022.

Doan, V.Q., Kusaka, H., Nguyen, T.M., 2019. Roles of Past, Present, and Future Land Use and Anthropogenic Heat Release Changes on Urban Heat Island Effects in Hanoi, Vietnam: Numerical Experiments with a Regional Climate Model[j]. Sustainable Cities and Society 47, 101479. https://doi.org/10.1016/j.scs.2019.101479.

Ferretti, A., Prati, C., Rocca, F., 2001. Permanent scatterers in SAR interferometry. IEEE Trans Geosci Remote Sens 39 (1), 8–20.

Giannaros, T.M., Melas, D., Daglis, I.A., Keramitsoglou, I., Kourtidis, K., 2013. Numerical Study of the Urban Heat Island over Athens (Greece) with the WRF Model[j].‘‘. Atmos Environ 73, 103–111.

Golden, J.S., Carlson, J., Kaloush, K.E., Phelan, P., 2007. A comparative study of the thermal and radiative impacts of photovoltaic canopies on pavement surface temperatures. Sol. Energy 81 (7), 872–883. https://doi.org/10.1016/j.

Goldstein, R.M., Werner, C.L., 1998. Radar interferogram filtering for geophysical applications. Geophys. Res. Lett 25 (21), 4035–4038.

Haji-Aghajany, S., Amerian, Y., 2018. An investigation of three dimensional ray tracing method efficiency in precise point positioning by tropospheric delay correction. Journal of Earth and Space Physics 44, 39–52. 10.22059/JESPHYS.2018.236885.1006913.

Haji-Aghajany, S., Amerian, Y., 2020a. Atmospheric phase screen estimation for land subsidence evaluation by InSAR time series analysis in Kurdistan. Iran. J. Atmos. Sol. Terr. Phys. 205, 105314. https://doi.org/10.1016/j.jastp.2020.105314.

Haji-Aghajany, S., Amerian, Y., 2020b. Assessment of InSAR tropospheric signal correction methods. J. Appl. Remote Sens. 14, 044503. https://doi.org/10.1117/1.JRS.14.044503.

Haji-Aghajany, S., Pirooznia, M., Raoofian Naeeni, M., Amerian, Y., 2020. Combination of Artificial Neural Network and Genetic Algorithm to Inverse Source Parameters of Sefid-Sang Earthquake Using InSAR Technique and Analytical Model Conjunction. Journal of the Earth and Space Physics 45 (4), 121–131. 10.22059/JESPHYS.2019.269596.1007065.

Haji-Aghajany, S., Amerian, Y., Verhagen, S., Rohm, W., Schuh, H., 2021. The effect of function-based and voxel-based tropospheric tomography techniques on the GNSS positioning accuracy. J. Geod. 95, 78. https://doi.org/10.1007/s00190-021-01528-2.

Haji-Aghajany, S., Amerian, Y., Amiri-Simkooei, A., 2022. Function-Based Troposphere Tomography Technique for Optimal Downscaling of Precipitation. Remote Sens. 14, 2548.

Haji-Aghajany, S., Amerian, Y., Amiri-Simkooei, A., 2023. Impact of climate change parameters on groundwater level: Implications for two subsidence regions in Iran using geodetic observations and artificial neural networks (ANN). Remote Sensing 15 (6), 1555. https://doi.org/10.3390/rs15061555.

Haji-Aghajany, S. (2021). Function-Based Troposphere Water Vapor Tomography Using GNSS Observations. PhD Thesis, Faculty of Geodesy and Geomatics Engineering, K. N. Toosi University of Technology.

Hanssen, R.F., 2001. Radar interferometry: Data interpretation and error analysis. Springer Science & Business Media, Heidelberg 2, 308. https://doi.org/10.1007/0-306-47633-9.

He, Q., Shen, Z., Wan, M., Li, L., 2020. Precipitable Water Vapor Converted from GNSS-ZTD and ERA5 Datasets for the Monitoring of Tropical Cyclones[j]. IEEE Access 8, 87275–87290. https://doi.org/10.1109/ACCESS.2020.2991094.

Hooper, A. J. (2005), Persistent scatter radar interferometry for crustal deformation studies and modeling of volcanic deformation.

Iacono, M.J., Delamere, J.S., Mlawer, E.J., Shephard, M.W., Clough, S.A., Collins, W., 2008. Radiative forcing by long-lived greenhouse gases: Calculations with the AER radiative transfer models. J. Geophys. Res. Space Phys. 113, 13103. https://doi.org/10.1029/2008jd009944.

Izanlou, A.S., Haji-Aghajany, B.S., Amerian, C.Y., 2024. Enhanced Troposphere Tomography: Integration of GNSS and Remote Sensing Data with Optimal Vertical Constraints. IEEE Journal of Selected Topics in Applied Earth Observations and Remote Sensing.

Khalili, M.A., Guerriero, L., Pouralizadeh, M., Calcaterra, D., Di Martire, D., 2023a. Monitoring and prediction of landslide-related deformation based on the GCN-LSTM algorithm and SAR imagery. Natural Hazards 119 (1), 39–68.

Khalili, M.A., Voosoghi, B., Guerriero, L., Haji-Aghajany, S., Calcaterra, D., Di Martire, D., 2023b. Mapping of mean deformation rates based on APS-corrected InSAR data using unsupervised clustering algorithms. Remote Sensing 15 (2), 529. https://doi.org/10.3390/rs15020529.

Kleerekoper, L., Van Esch, M., Salcedo, T.B., 2012. How to make a city climate-proof, addressing the urban heat island effect. Resources, Conservation and Recycling 64, 30–38.

Kondo, K., Mabon, L., Bi, Y., Chen, Y., Hayabuchi, Y., 2021. Balancing Conflicting Mitigation and Adaptation Behaviours of Urban Residents under Climate Change and the Urban Heat Island Effect[j]. Sustainable Cities and Society 65, 102585. https://doi.org/10.1016/j.scs.2020.102585.

Li, Z., Fielding, E.J., Cross, P., Muller, J.-P., 2006. Interferometric synthetic aperture radar atmospheric correction: GPS topography-dependent turbulence model. J. Geophys. Res. 111, B02404. https://doi.org/10.1029/2005JB003711.

Liu, Y., Li, T., Yu, L., 2020. Urban Heat Island Mitigation and Hydrology Performance of Innovative Permeable Pavement: A Pilot-Scale Study[j]. J. Clean. Prod 244, 118938. https://doi.org/10.1016/j.jclepro.2019.118938.

Maddahi, S., Tasan, M., Haji-Aghajany, S., 2023. Enhancing InSAR accuracy: Unveiling more accurate displacement fields through 3-D troposphere tomography. Journal of Atmospheric and Solar-Terrestrial Physics 256. https://doi.org/10.1016/j.jastp.2024.106207.

Massonnet, D., Feigl, K.L., 1998. Radar interferometry and its application to changes in the Earth's surface. Rev. Geophys 36 (4), 441–500.

Memon, R.A., Leung, D.Y.C., Liu, C.-H., 2009. An investigation of urban heat island intensity (UHII) as an indicator of urban heating. Atmos. Res. 94 (3), 491–500. https://doi.org/10.1016/j.atmosres.2009.07.006.

Mendes B.V, Langley R.B. (1998), Tropospheric zenith delay prediction accuracy for airborne gps high-precision positioning Proceedings of The Institute of Navigation 54th Annual Meeting, pp. 337-34.

Mendez-Astudillo, J., Lau, L., Tang, Y.-T., Moore, T., 2021. A New Global Navigation Satellite System (GNSS) Based Method for Urban Heat Island Intensity Monitoring [j]. Int J Appl Earth Obs Geoinf 94, 102222. https://doi.org/10.1016/j.jag.2020.102222.

Meyer, F. J., & Nicoll, J. (2008), The impact of the ionosphere on interferometric SAR processing. In IGARSS 2008-2008 Int. Geosci. Remote Sens. Symp (Vol. 2, pp. II-391). IEEE.

Michalakes, J.; Dudhia, J.; Gill, D.; Henderson, T.; Klemp, J.; Skamarock, W.; Wang, W. (2004), The Weather Research and Forecast Model: Software Architecture and Performance. In Proceedings of the 11th ECMWF Workshop on the Use of High Performance Computing in Meteorology, 25−29 October, 2004; Mozdzynski, G. Ed.; Reading: Redding, UK.

Miele, P., Di Simone, A., Khalili, M.A., Palumbo, S., Di Martino, G., Di Martire, D., 2023. Integrated Infrastructure Monitoring Procedure for Road Network Management. In: IGARSS 2023–2023 IEEE International Geoscience and Remote Sensing Symposium. IEEE, pp. 3648–3651.

Mirzaei, P.A., 2015. Recent Challenges in Modeling of Urban Heat Island[j]. Sustainable Cities and Society 19, 200–206. https://doi.org/10.1016/j.scs.2015.04.001.

Moriasi, D.N., Arnold, J.G., van Liew, M.W., Bingner, R.L., Harmel, R.D., Veith, T.L., 2007. Model evaluation guidelines for sys-tematic quantification of accuracy in watershed simulations. Trans. ASABE 50, 885–900.

Nakanishi, M., Niino, H., 2006. An improved Mellor-Yamada level-3 model: Its numerical stability and application to a regional prediction of advection fog. Bound.-Layer Meteorol 119, 397–407.

Nilsson, T., Böhm, J., Wijaya, D.D., Tresch, A., Nafisi, V., Schuh, H., 2013. Path Delays in the Neutral Atmosphere. Springer, Berlin/Heidelberg, Germany, pp. 73–136.

Niu, G.-Y., Yang, Z., Mitchell, K.E., Chen, F., Ek, M.B., Barlage, M., Kumar, A., Manning, K., Niyogi, D., Rosero, E., et al., 2011. The community Noah land surface model with multiparameterization options (Noah-MP): 1. Model description and evaluation with local-scale measurements. J. Geophys. Res. Space Phys. 116 https://doi.org/10.1029/2010jd015139.

Onn, F., Zebker, H.A., 2006. Correction for interferometric synthetic aperture radar atmospheric phase artifacts using time series of zenith wet delay observations from a GPS network. J. Geophys. Res. 111, B09102. https://doi.org/10.1029/2005JB004012.

Pathak, C., Chandra, S., Maurya, G., Rathore, A., Sarif, M.O., Gupta, R.D., 2021. The Effects of Land Indices on Thermal State in Surface Urban Heat Island Formation: A

Case Study on Agra City in India Using Remote Sensing Data (1992–2019)[J]. Earth Syst. Environ 5 (1), 135–154. https://doi.org/10.1007/s41748-020-00172-8.
Rodríguez, L.R., Ramos, J.S., de la Flor, F.J.S., Álvarez Domínguez, S., 2020. Analyzing the Urban Heat Island: Comprehensive Methodology for Data Gathering and Optimal Design of Mobile Transects[j]. Sustainable Cities and Society 55, 102027. https://doi.org/10.1016/j.scs.2020.102027.
Saastamoinen, J., 1973. Contributions to the theory of atmospheric refraction. Part II: refraction corrections in satellite geodesy. BullGeod 107, 13–34.
Savannah, GA.W., X., X. Yang, and G. Hu, 2011. Relationship between Land Cover Ratio and Urban Heat Island from Remote Sensing and Automatic Weather Stations Data [j]. J. Indian Soc. Remote Sens 39 (2), 193–201. https://doi.org/10.1007/s12524-011-0076-4.
Sobrino, J.A., Oltra-Carrió, R., Sòria, G., Bianchi, R., Paganini, M., 2012. Impact of Spatial Resolution and Satellite Overpass Time on Evaluation of the Surface Urban Heat Island Effects[j]. Remote Sens. Environ 117, 50–56. https://doi.org/10.1016/j.rse.2011.04.042.
Statistical Center of Iran (2018), Available online: http://www.amar.org.ir.
Stewart, I.D., Oke, T.R., 2012. Local climate zones for urban temperature studies. Japan Meteorological Agency. Surface Observation. Available online: Bull. Am. Meteorol. Soc. 93, 1879–1900 https://www.jma.go.jp/jma/en/Activities/surf/surf.html.
Stewart, I.D., Oke, T.R., Krayenhoff, E.S., 2014. Evaluation of the 'local climate zone' scheme using temperature observations and model simulations. Int. J. Climatol. 34, 1062–1080.
Susca, T., Pomponi, F., 2020. Heat Island Effects in Urban Life Cycle Assessment: Novel Insights to Include the Effects of the Urban Heat Island and Uhi-mitigation Measures in LCA for Effective Policy Making[j]. J. Ind. Ecol 24 (2), 410–423. https://doi.org/10.1111/jiec.12980.
Tasan, M., Ghorbaninasab, Z., Haji-Aghajany, S., Ghiasvand, A., 2023. Leveraging GNSS tropospheric products for machine learning-based land subsidence prediction. Earth Science Informatics 16 (4), 3039–3056.
Tehran Times (2023), Iran's Mashhad air pollution levels exceed standards, https://www.tehrantimes.com/news/474725/Iran-s-Mashhad-air-pollution-levels-exceed-standards.
Thompson, G., Field, P.R., Rasmussen, R.M., Hall, W.D., 2008. Explicit forecasts of winter precipitation using an improved bulk microphysics scheme. Part II: Implementation of a new snow parameterization. Mon. Weather Rev 136, 5095–5115.
Tolman, B.W. (2008), GPS precise absolute positioning via Kalman filtering. In: Paper Presented at the ION GNSS 21st International Technical Meeting of the Satellite Division. Savannah, GA. Division.
Xia, P., Peng, W., Yuan, P., Ye, S., 2024. Monitoring urban heat island intensity based on GNSS tomography technique. Journal of Geodesy 98 (1), 1.
Zebker, H.A., Rosen, P.A., Hensley, S., 1997. Atmospheric effects in interferometric synthetic aperture radar surface deformation and topographic maps. J. Geophys. Res: Solid. Earth 102(B4):7547{7563.